ORIGINAL ARTICLE

Experimental evaluation of rotational and traverse speeds effects on corrosion behavior of friction stir welded joints of aluminum alloy AA5052-H32

Roosvel Soto-Díaz[1] · Anderson Sandoval-Amador[2,3] · Jimy Unfried-Silgado[4]

Abstract

In this study, relationships among process parameters, traverse and rotation speed, and the corrosion resistance at stir region of friction stir welded joints of aluminum alloy AA5052-H32 were evaluated, which were obtained using a tool with featured shoulder and threaded pin. Corrosion analysis was carried out using open circuit potential (OCP) potentiodynamic polarization curves and electrochemical impedance spectroscopy (EIS) tests in a 3.5% (w/v) NaCl solution. Optical microscopy, scanning electron microscopy, and chemical microanalysis were used aiming to study corroded regions. Using a statistical design test completely randomized, complemented by characterization of microstructure evolution and equivalent circuit analysis, there have been correlated welding parameters and corrosion resistance. The resistance of pitting corrosion was associated with grain refinement, heat input, and passivation at stir region for all parameter combinations. Results showed than parameter combination 700 rpm and 100 mm.min^{-1} exhibited higher corrosion resistance and mechanical properties compared to other used parameters

1 Introduction

AA5xxx series aluminum alloys are a group of solid-solution strengthening Al-Mg alloys, non-heat treatable, strain hardenable, bringing high mechanical properties with good corrosion resistance both in seawater and marine environment, good formability, acceptable high temperature fatigue properties, appreciable fracture resistance and good weldability [1–5]. Typically AA5052 alloy contents between 2.2 and 2.8

✉ Jimy Unfried-Silgado
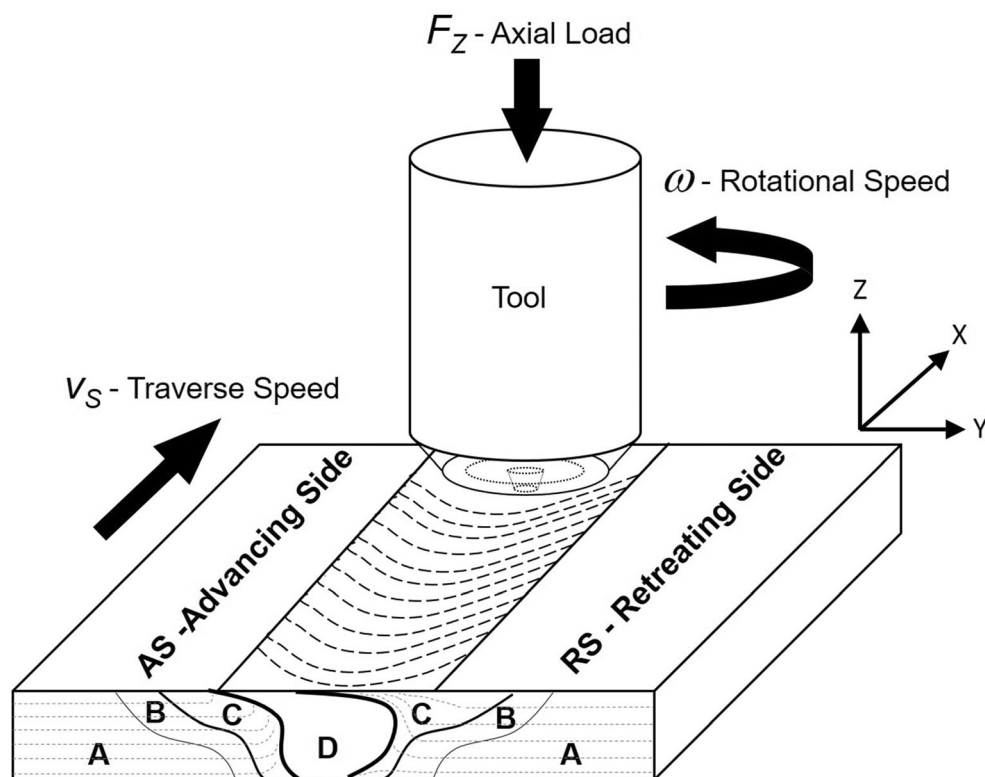jimyunfried@correo.unicordoba.edu.co

1 Universidad Autónoma del Caribe. Ingeniería Mecánica. Grupo IMTEF, Barranquilla, Colombia

2 Instituto de Física Arroyo Seco, Universidad Nacional del Centro de la Provincia de Buenos Aires, Pinto 399, C.P. 7000, Tandil, Buenos Aires, Argentina

3 Foundation for Researchers in Science and Technology of Materials – FORISTOM, C.P, 680003 Bucaramanga, Santander, Colombia

4 Universidad de Córdoba. Departamento de Ingeniería Mecánica. Grupo ICT, Carrera 6ta No. 77-305, ZIP: 230002 - Bloque 32 Montería, Colombia

%-wt of Mg, 0.15 to 0.35 %-wt of Cr, <0.40%-wt of Fe, Si, and Mn, which are widely used in manufacturing of light-weight transportation vehicles, ships, sheet metal parts, fuel tanks, electrical shells, molds, hardware products, dies, among others parts [6, 7]. Weldability of AA5052 alloys is acceptable using arc-based fusion welding processes like as GTAW and GMAW, and more recently hybrid processes including laser combinated with the aforementioned processes [8, 9]. Nevertheless, problems associated to selective vaporization and volatilized depletion of alloying elements, especially magnesium, leading to porosities formation in the fusion zone [10]. Besides abovementioned problems are added grain coarsening due to recrystallization in the heat-affected zone (HAZ) and precipitation of undesirable second phases, which carry out to inevitable reduction of both mechanical properties and corrosion resistance in this kind of welded joints [11, 12].

Currently, several problems related to weldability of AA5052 using fusion welding processes have been mainly solved using friction stir welding (FSW). This solid-state welding process avoids difficulties arise from fusion, solidification effects, and higher thermal cycles associated to arc welding processing [13]. In FSW process parameter combinations (see Fig. 1), they cause high plastic deformation rate in

stir region, producing positive effects on grain size, second phase precipitations control in both heat-affected zone (HAZ) and thermomechanically affected zone (TMAZ), and lower mechanical properties reduction is more than the traditional fusion welding processes [14, 15]. The best FSW process window is established aiming to obtain acceptable mechanical properties, good texture, and free defects welded joints with lower reduction of hardness in stir region. For FSW of AA5052, the best range of parameters is rotational speed between 500 and 1500 rpm and traverse speed between 50 and 200 mm.min^{-1}, tilt angle range of 0 to 2°, and axial force of 5 to 10 kN [13, 16–18]. Typical values of mechanical properties of AA5052-H32 alloy in as-received state are 65-70 VHN for hardness, 228 and 193 MPa for ultimate and yield strength, respectively, and 12 to 18 % for strain elongation [19]. The AA5052-H32 friction stir welded joints using the abovementioned range of parameters could lead to a reduction of tensile properties and hardness between 5 and 30%, respectively, furthermore, a 15 to 20 % increase of elongation, meanly owing to recrystallization phenomena and heat input [2, 3, 20, 21].

Table 1 Chemical composition of AA5052-H32

Elements	Al	Mg	Fe	Cr	Si	Mn	Cu
wt.%	Bal.	2.21	0.216	0.155	0.07	0.038	0.004

Corrosion behavior of as-received AA5052-H32 has been experimentally determined in several works. The abovementioned representative electrochemical parameter values of corrosion potential (E_{corr}) and current density (I_{corr}) in NaCl solution are among −600 to −1200 mV, and 6 to 9 μA·cm^{-2}, respectively [22–24]. Changes induced by thermal cycles and deformation during welding on different welding regions, and according to strain hardened state of studied material, could modify the corrosion resistance in welded joints, exhibiting lower values than base metal [10, 24]. In AA5052-H32 friction stir welded joints, the corrosion problems are focused in rising up pitting corrosion more than stress corrosion cracking in the stir, thermomechanically affected, and heat-affected zones regarding base metal [24]. Several works deal with behavior corrosion in friction stir welded joints of AA5052; however, there are very little studies on behavior corrosion in friction welded joints of AA5052-H32, and almost none of them considering featured shoulder and threated pin tools. Most of those investigations have used AA5052 in annealed state, establishing relationships among, FSW process parameters, mechanical properties, microstructure observations, potentiostatic, and electrochemical impedance spectroscopy studies in the welding regions [25, 26].

Shamsudeen and Dhas studied mechanical properties and corrosion of FSW welded joints of AA5052 developed using a tapered square tool pin profile, flat shoulder, a tool tilt angle of 1.5°, rotational speed of 600 rpm, welding speed of 65 mm/min, and axial load of 7 kN [24]. Results showed that an

Table 2 Tool dimensions and process parameters

Identification	Traverse speed (mm/min)	Rotational speed (rpm)	R (mm·rev^{-1})
FSW-A	50	500	0.100
FSW-B	75	600	0.125
FSW-C	100	700	0.140

ultimate strength joint efficiency > 92 % was obtained. Moreover, corrosion potential (E_{corr}) and current density (I_{corr}) in 3.5 % NaCl of this welded joints were −0.85 V and 1.2 μA·cm^{-2}, respectively, showing an important reduction I_{corr} and concentration of pitting corrosion at stir zone. Similar results were observed in others works, which were focused on FSW of AA5052 without establish kind of treatment that was studied [10, 26, 27]. The aforementioned works did not link precipitation of second phases with behavior corrosion of FSW welded joints. On the other hand, friction stir welded joints were developed using combination of featured shoulder and conical threaded pin that could lead to lower deformation, higher heat input stability, and extensively grain refinement at stir region in aluminum, owing to increase both frictional and plasticizer heat during process [28, 29]. These abovementioned behaviors suggest that the stir region microstructure of AA5052-H32 changes during FSW, then its corrosion resistance could be affected, which will result interesting to study, since it has not been widely reported. The goal of this work is to determine the influence of process parameters, rotation speed, and traverse speed on behavior of corrosion of friction stir welded joints of aluminum alloy AA5052-H32, which were obtained using a featured shoulder and threaded conical pin tool. Aiming to reach this goal, this work expected to obtain free defects welded joints with appropriate combinations of process parameters, developing tensile and hardness testing, microstructure characterization, and corrosion

testing based on potentiodynamic and electrochemical impedance spectroscopy measurements on stir region.

2 Materials and methods

2.1 Materials

Commercial plates of aluminum alloy AA5052-H32 with dimensions of 150 mm × 75 mm × 3 mm were used as base metal in this work and which chemical composition was determined using spectroscopy, and it is shown in Table 1.

2.2 Welding process parameters and performance

Butt welded joints were obtained in parallel direction to rolled direction of base metal plates using a skilled FSW equipment TTI® model RM1. The tool was manufactured in H13 steel and designed with a trifluted conical threaded pin and a featured shoulder with spirals with ∅ 13 mm of diameter, which is shown in Fig. 2. During the welding process, a tool tilt angle of 2 ° was used. Process parameters were selected according to referenced literature information. Tool geometrical details and dimensions as well as the selected process parameters in the implementation of the welding process are shown in Table 2.

Thermal cycles were measured in function of elapsed time using type K thermocouples arranged in the tool shoulder's.
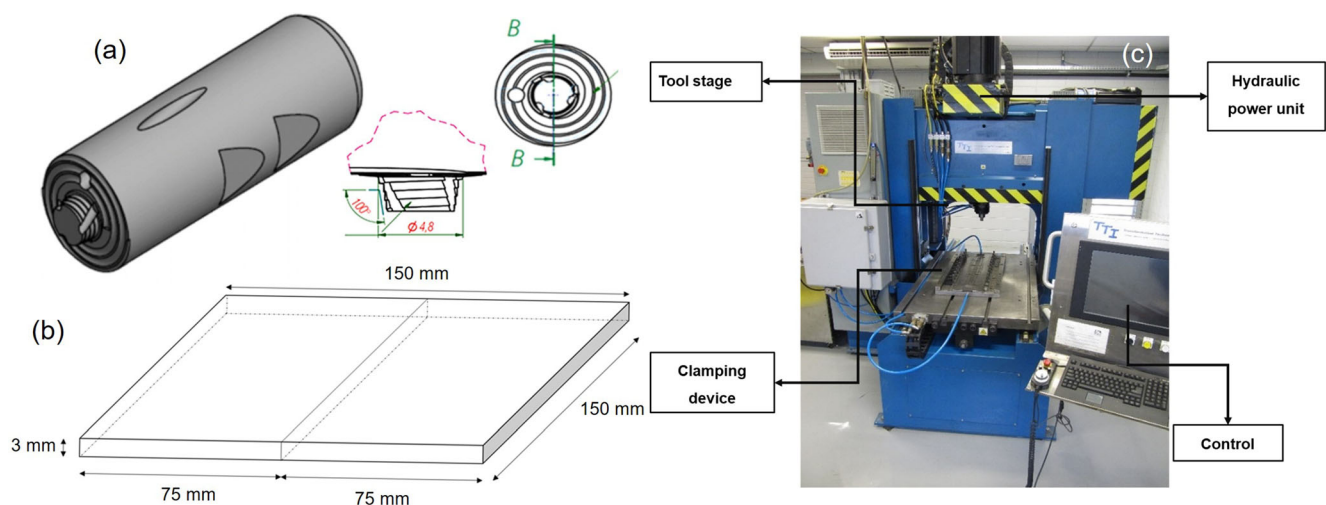
Fig. 2 (a) Geometrical and dimensions of used tool. (b) Detail of welded joint dimensions. (c) Experimental setup
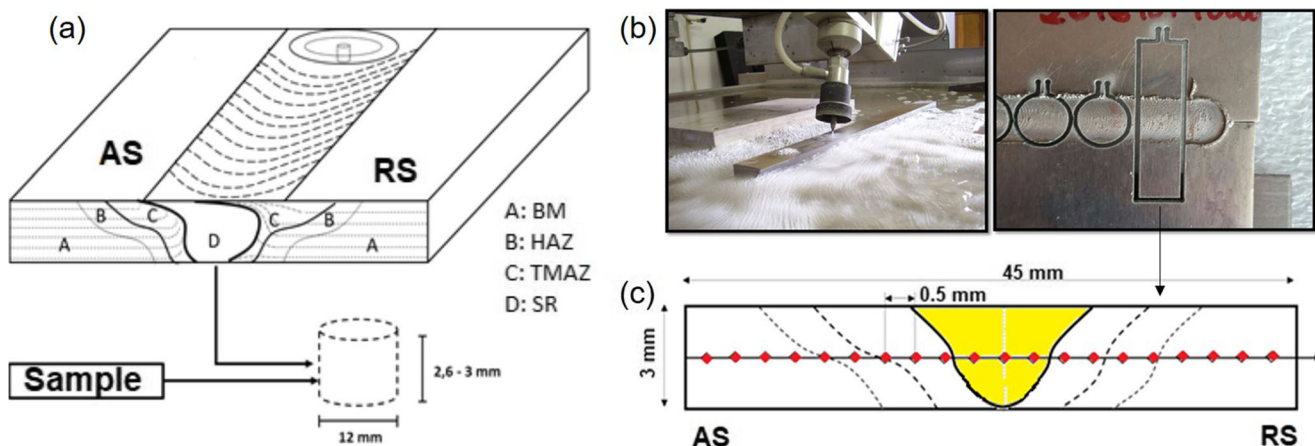
Fig. 3 (a) Location of extracted corrosion samples. (b) Cutting of corrosion samples. (c) Microhardness cross-section profile

These data were used to show thermal history in stirred zone during the process.

2.3 Microstructure characterization

Base metal and welded joint specimens were cut from perpendicular section to weld direction. Soon, sectioned specimens were metallographically prepared with standard procedures and polished with alumina of 1, 0.5, and 0.05 μm. Polished specimens were etched with ASTM 407 reagent Keller's (2 ml HF + 3 ml HCl + 5 ml HNO_3 + 100 ml distilled water). Microstructures of base metal, welded, and corroded specimens were examined using optical microscopy (OM) through an Olympus BX51 microscope, and a JEOL FEG JSM-7100 SEM FEG microscope coupled with silicon drift detector EDS analysis.

2.4 Microhardness measurements

Vickers microhardness test was developed following ASTM E384-11 standard and using a Shimadzu 4049 microdurometer with 100 gf of load during 10 s. Microhardness cross-section

profiles were made in the middle zone of welded joints, as is shown in Fig. 3. A total 30 indentations on each sample were developed using 0.5 mm between each one, starting from the center of the weld towards the advanced and retrieved sides, respectively.

2.5 Corrosion tests

Cylindrical samples were extracted from stir region by each welding tested condition using a water jet cutter and its dimensions are showed in Fig. 3. Corrosion behavior of base metal and welded specimens was analyzed by potentiodynamic techniques and electrochemical impedance spectroscopy (EIS). Electrochemical tests were performed using a three-electrode cell containing 3.5 % NaCl solution open to the air at 25 ± 1 °C, using a Gamry® 600 potentiostat. Electrochemical cell consisted of a working electrode which was formed by tested sample, an Ag/AgCl (3 M KCl) as reference electrode, and a high purity graphite stick, which were considered as counter electrode. Exposed area for electrochemical tests was kept in 0.65 cm^2. Open circuit delay (OCD) time was kept in 6000 s. Process parameters for the

Fig. 4 (a) Microstructure arrangement of as-received base material. (b) Detail of β precipitates observed in traverse direction
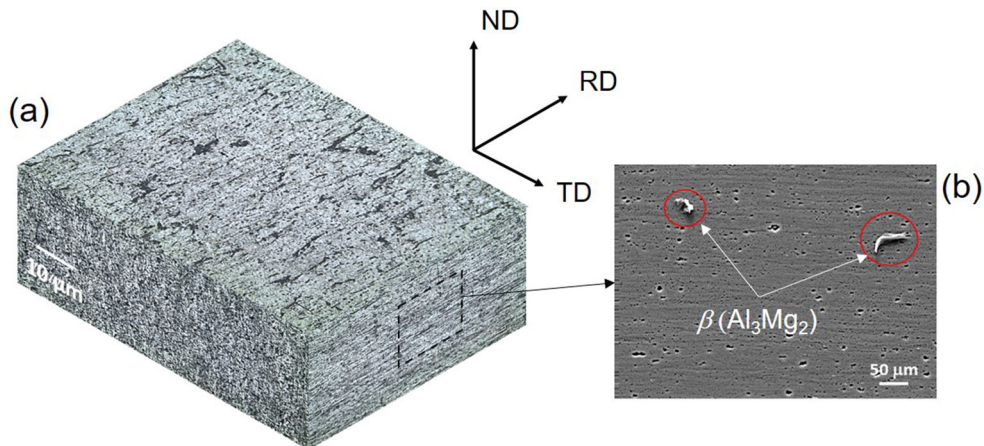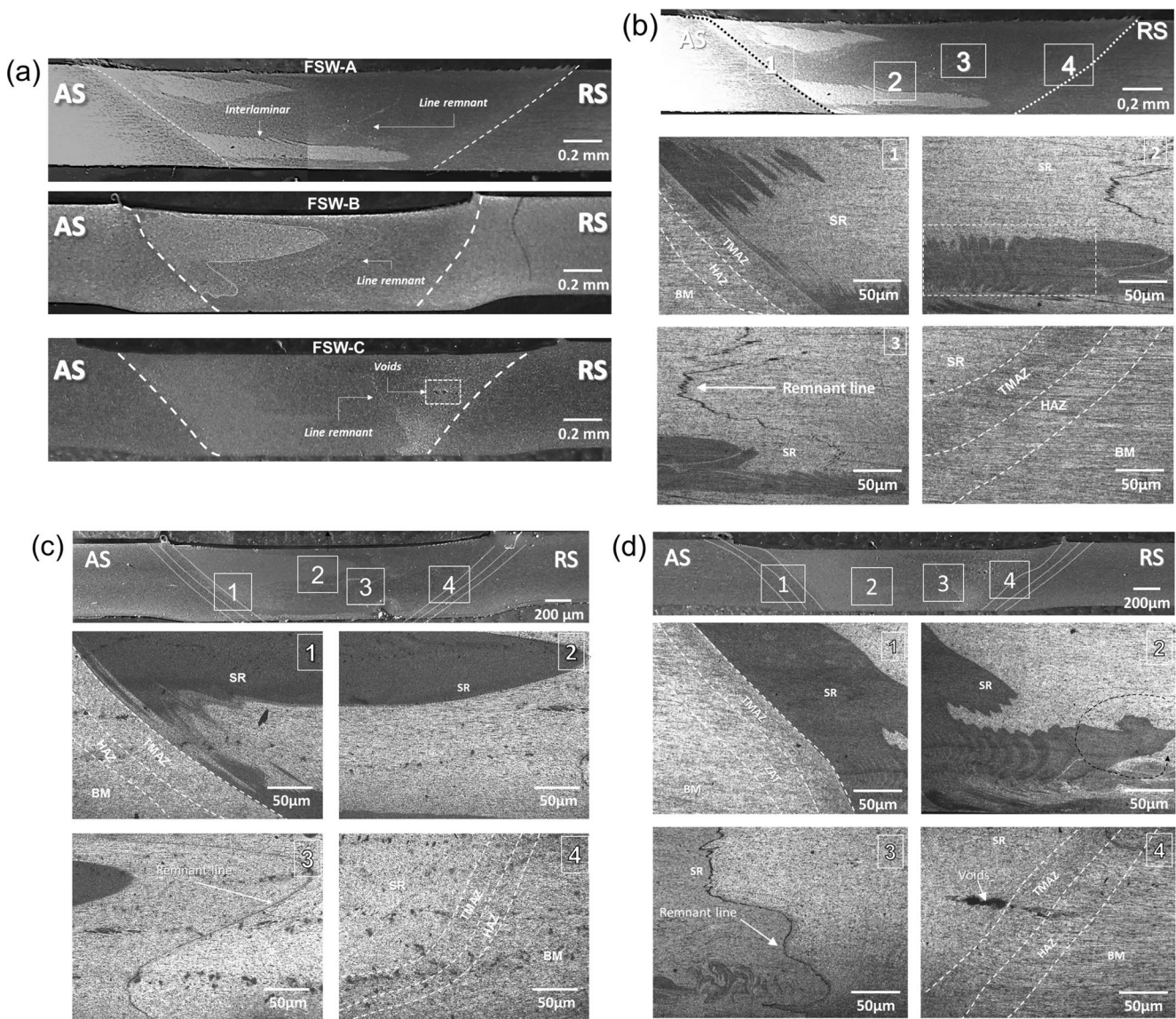
Fig. 5 (a) Image shows the macroscopic details of welded joints. (b) Image shows details of different welded regions in FSW-A (50 mm.min^{-1} — 500 rpm). (c) Image shows details of different welded regions in FSW-B (75 mm.min^{-1} — 600 rpm). (d) Image shows details of different welded regions in FSW-C (100 mm.min^{-1} — 700 rpm). AS, advanced side. RS, retreated side

Tafel polarization test were potential range −300 mV to + 300 mV with respect to open circuit potential (OCP), and there was used a scanning rate of 1 mV·s^{-1}. EIS measurements were carried out in a frequency range from 1 mHz up to 100 KHz, recording 7 points per decade and applying a perturbation signal of 5 mV$_{rms}$. Spectra were processed using equivalent circuit of Randles. Corroded samples were observed and analyzed by scanning electron microscopy and EDS analysis.

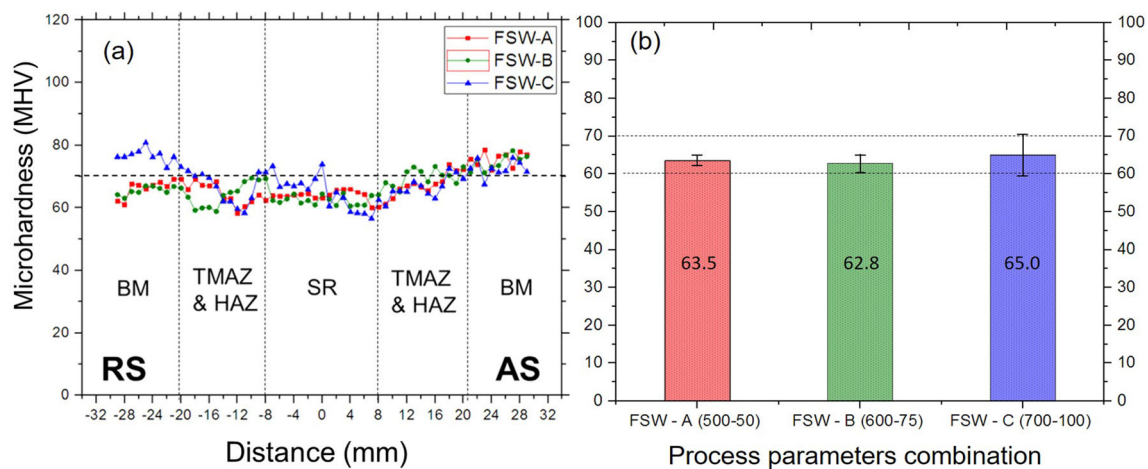| Table 3 Summary of results of experimental and calculated welding parameters	Sample	ω (rpm)	v (mm·min^{-1})	Ratio		Peak of temperature (°C)	Torque (N·m)	Heat input (kJ·mm^{-1})	Tendency of grain size
				ω/v	ω/v^2				
	FSW A	500	50	10	5000	367.1	48.7	3.1	Coarsening
	FSW B	600	75	8	4800	366.9	39.7	2.0	Average
	FSW C	700	100	7	4900	327.6	35.7	1.6	Refinement

Fig. 6 (a) Microhardness cross-section profiles and (b) average microhardness values at stir region in function of process parameters

3 Results and discussion

In Fig. 4, the results of microstructure characterization of base metal in as-received state are shown. Microstructure is formed by elongated grains at rolling (RD) and normal (ND) directions, whereas traverse direction (TD) shows equiaxed grains, which were produced by perpendicular cut of elongated grains, and these results are coherent with those observed in other works [16, 30]. In base metal, diverse kinds of second phase precipitates are expected; however, only β - Al_3Mg_2 precipitates were observed using microscopy characterization [2]. In Fig. 5a, the cross section of welded joints obtained using experimental conditions displayed in Table 2 is shown. Welded joints obtained under conditions –A and –B were free voids and porosities, whereas –C condition showed voids near to the retreated side. All welded joints displayed remnant lines in stir region [31], while welded joint under –A condition exhibited interlaminar regions before onion ring structure at stir region [29], due to low heat input generated by welding parameters, as it was observed in another work [13]. Figures 5b to 5d show comparative details of microstructure of welded joints, displaying identified different characteristics and welding regions.

In Table 3, the results of spindle torque and peak of temperature experimentally measured during the welding process in function of used process parameters are summarized. Also, it is shown the calculated heat input (HI), which has been estimated using Eq. (1), where ω is rotational speed, τ is spindle torque, and v is traverse speed [32].

$$HI = \frac{2\pi\omega\tau}{1000v} \; [kJ \cdot mm^{-1}] \tag{1}$$

In Table 3, the tendency of grain size at stir region in function of used welding process parameters is shown. An appropriate combination of rotation speed ω and traverse speed v

helps to generate a suitable level of free defects and recrystallization at stir region [33]. It is well known that the maximum peak of temperature at stir region is obtained when the ratio $\omega.v^{-2}$ is increased [34], while the torque value decreases when the ratio $\omega \cdot v^{-1}$ decreases. Torque and peak temperature measurements obtained in this work were coherent with both relationships established. Calculated heat input was proportional to ratio $\omega \cdot v^{-1}$, which together with strengthened state of base material before of welding, there have generated the tendency of grain size at stir region showed in Table 3. The abovementioned tendency has been experimentally corroborated in FSW welded joints of the AA5052-H32 in other works [13, 35]. Under these mentioned conditions, coarsened grains at stir region generated less grain boundaries than that one with refined grains, conditioning the behavior of corrosion and mechanical properties in welded joint [25]. Figure 6 shows microhardness cross-section profiles of welded joints experimentally measured. Results show that observed microhardness values under imposed experimental conditions vary between 60 and 70 VHN at stir region, which is in agreement with average hardness of base metal (68 ± 2 VHN), showing little variation of hardness because of process. Comparing the average microhardness value among evaluated conditions, it is observed that for condition FSW–C, it is lightly higher than others conditions, which was expected due to the structure of refined grains obtained there, according to the results showed in Table 3.

Figure 7 shows the comparison between base metal microstructure and stirred regions of welded joints obtained with –A, –B, and –C conditions, respectively. SEM images at × 1000 show that after the welding process there is a clear tendency to increase the precipitates at stir region, which is expected due to thermal and strain conditions. It was not possible to clearly reveal the grain size at stir regions probably due to the presence of precipitates [17, 21]. XRD results of these regions show low fraction of precipitates and a predominating
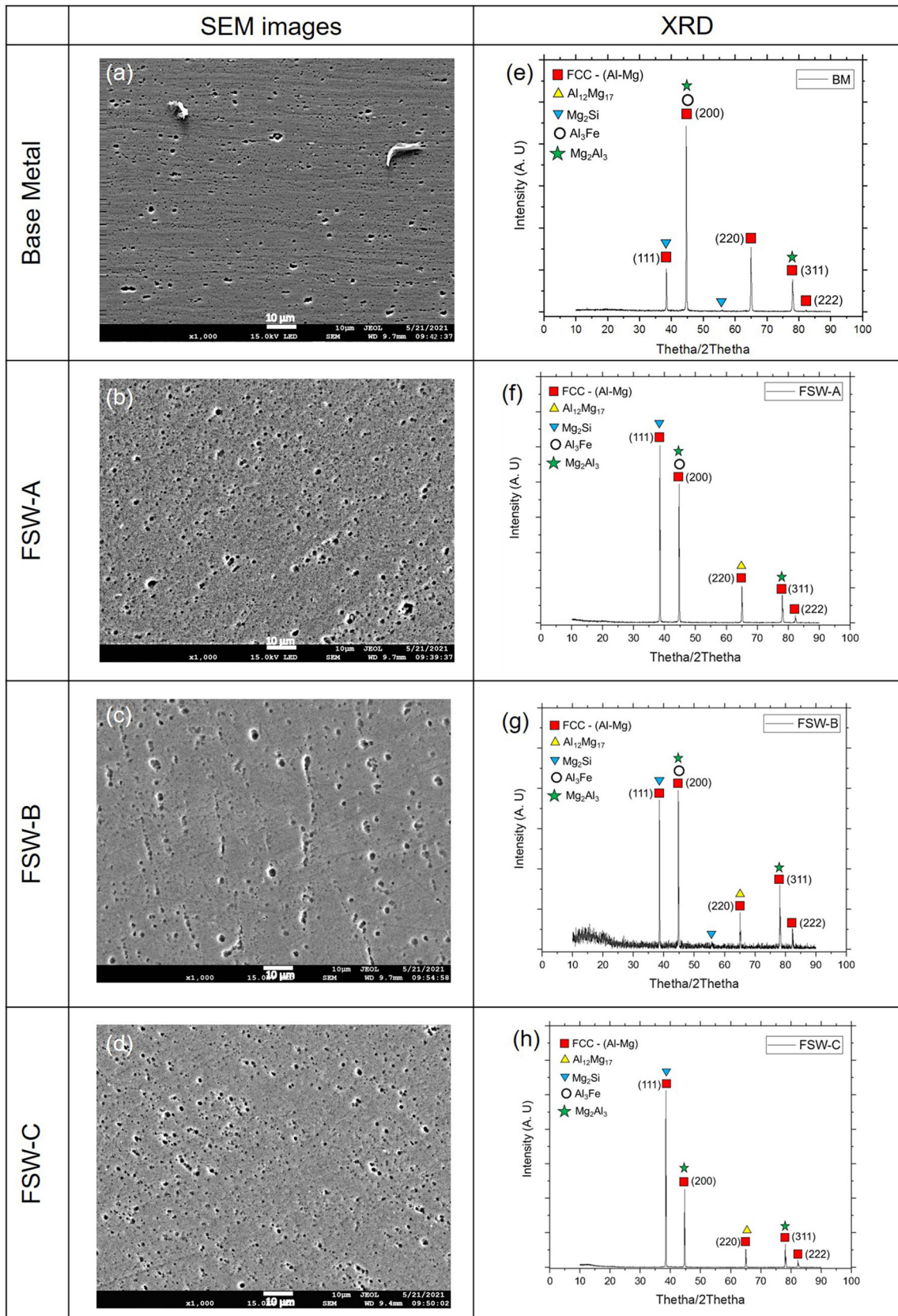
Fig. 7 Images of SEM-SE showing the comparison of microstructure among (a) base metal and stir regions of (b) FSW-A, (c) FSW-B, and (d) FSW-C samples. XRD results of (e) base metal and stir regions of (f) FSW-A, (g) FSW-B, and (h) FSW-C samples
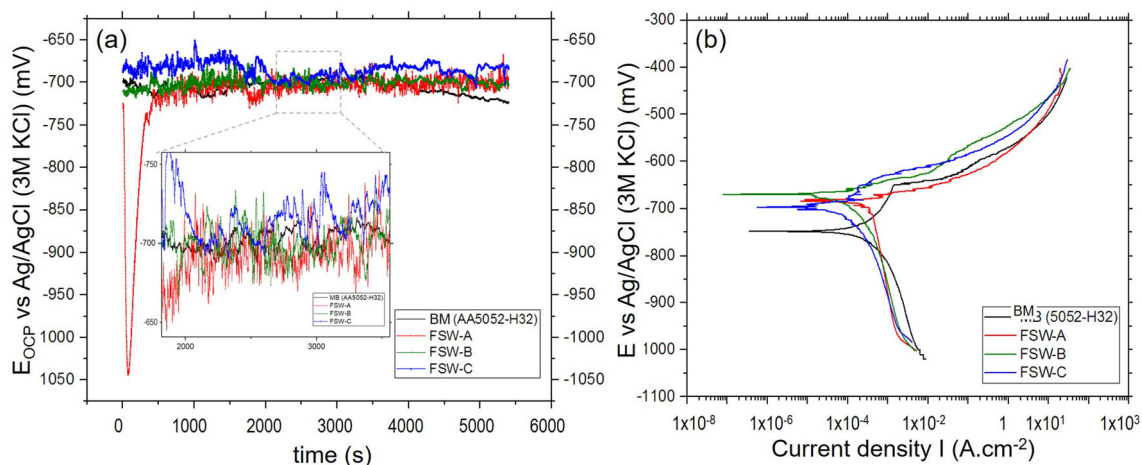
Fig. 8 (a) Open circuit potential and (b) potentiodynamic polarization curves measured in base metal, FSW-A, FSW-B, and FSW-C conditions. 3.5% NaCl electrolyte

FCC α-(Al-Mg) matrix. XRD results show prevalence of Al- and Mg-rich precipitates (Al_3Mg_2, Mg_2Si, and $Al_{12}Mg_{17}$) at stir regions. Using a qualitative analysis of XRD peaks of precipitates based on ratio signal/noise, it was observed that stir region of –C condition obtained higher ratio of Al_3Mg_2 and Mg_2Si precipitates, whereas Al_3Fe precipitates peak was not observed. On the other hand, stir region of –A condition showed higher ratio for Al_3Mg_2 and Al_3Fe precipitates.

In Fig. 8a, the results of open circuit potential (OCP) measurements are shown. Results showed that base metal and all evaluated experimental conditions presented a similar behavior, showing an oscillatory behavior of the potential value during the analyzed period. Relative to base metal measurements, an increase in OCP can be observed for all weld joint conditions. This increase can be attributed to the refinement of the grain size associated with the stirring speed [27].

In Fig. 8b and Table 4, potentiodynamic test results from base metal and evaluated welded joints are shown. Results show that cathodic branches were similar for all welded conditions and, in turn, these were slightly different to base metal. Anodic branch for base metal and condition -C exhibited two different areas. The first area had place matrix dissolution. Whereas, in the second area, an accelerated dissolution occurred, preferentially in Mg-rich locations [27]. Samples A and B show a typical behavior of clarified dissolution of the metallic matrix. Furthermore, anodic polarization behavior of

the curves evidenced a strong rising in dissolution current density without arrive to the passivation. The aforementioned behavior corresponds to pitting breakdown potential of duplex protective oxide film on AA5052 aluminum alloy, such as it was observed in other works [25, 27]. Results showed that corrosion potential E_{corr} in stir region for evaluated conditions is more positive than base metal. The aforementioned confirms that AA5052 is an inherently intergranular-resistant alloy. It is possible to explain these results from difference of grain size among BM and FSW conditions [25]. On the other hand, I_{corr} is lower in the condition –B when it is compared to other conditions, which is coherent with the lowest rate of corrosion in this condition, probably due to the smallest grain size produced by process parameters.

Figure 9 shows the Bode and Nyquist plots from the EIS measurements. Equivalent circuit used for each analysis was the simplified Randle's circuit, which is a reasonable approximation to behavior of stirred regions, since the interface to be analyzed is composed of a metallic surface and the saline solution [23, 27]. Analysis for Bode diagram results showed that stirred region of conditions –B and –C presented the highest values of impedance compared to base metal. A good correlation between grain size and impedance values was observed. Probably the grain refinement improved the response to corrosion in these cases [25]. In the Nyquist diagrams, the formation of almost perfect domes can be observed, which is a

Table 4 Electrochemical parameters obtained from the potentiodynamic polarization curves

| Sample condition	R (mm·min^{-1})	E_{corr} (mV)	I_{corr} (μA·cm^{-2})	CR (mpy) $\times 10^{-6}$
BM (5053-H32)	---	−742	−242	4.11
FSW-A	0.100	−685	−342	5.80
FSW-B	0.125	−669	−31.2	0.53
FSW-C	0.140	−697	−56.2	0.95

Table 5 Fitting parameters according to equivalent circuits

Sample	R_s (Ω)	R ($\Omega \cdot cm^2$)	$CPE - T \times 10^{-6}$ ($F \cdot cm^{-2}$)	$CPE - P$	χ^2
BM (5052-H32)	5.53	26,403	6.11	0.90	0.021
FSW-A	4.65	32,506	4.11	0.90	0.005
FSW-B	3.65	52,632	5.82	0.89	0.016
FSW-C	5.75	57,111	4.53	0.89	0.014
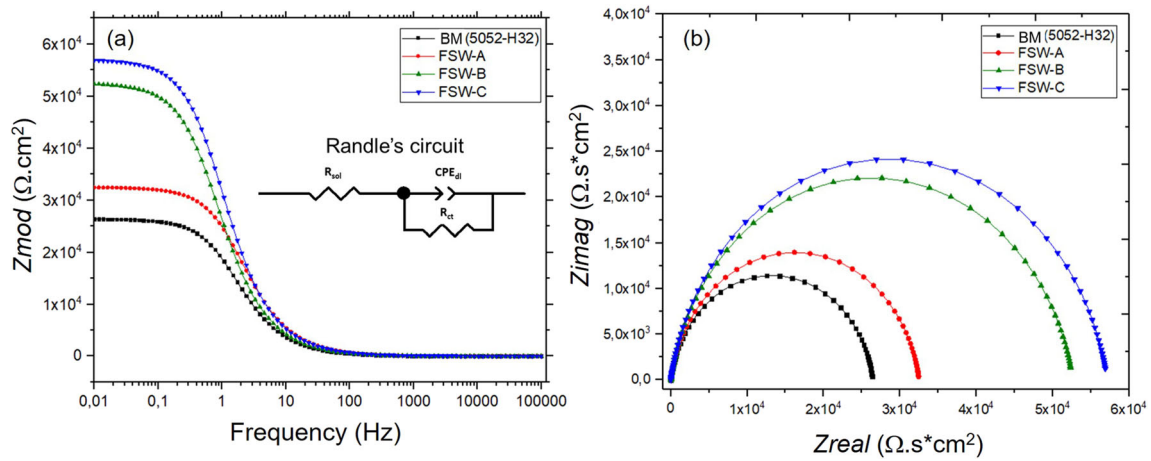
Fig. 9 Images show (a) Bode and (b) Nyquist plots from EIS measurements
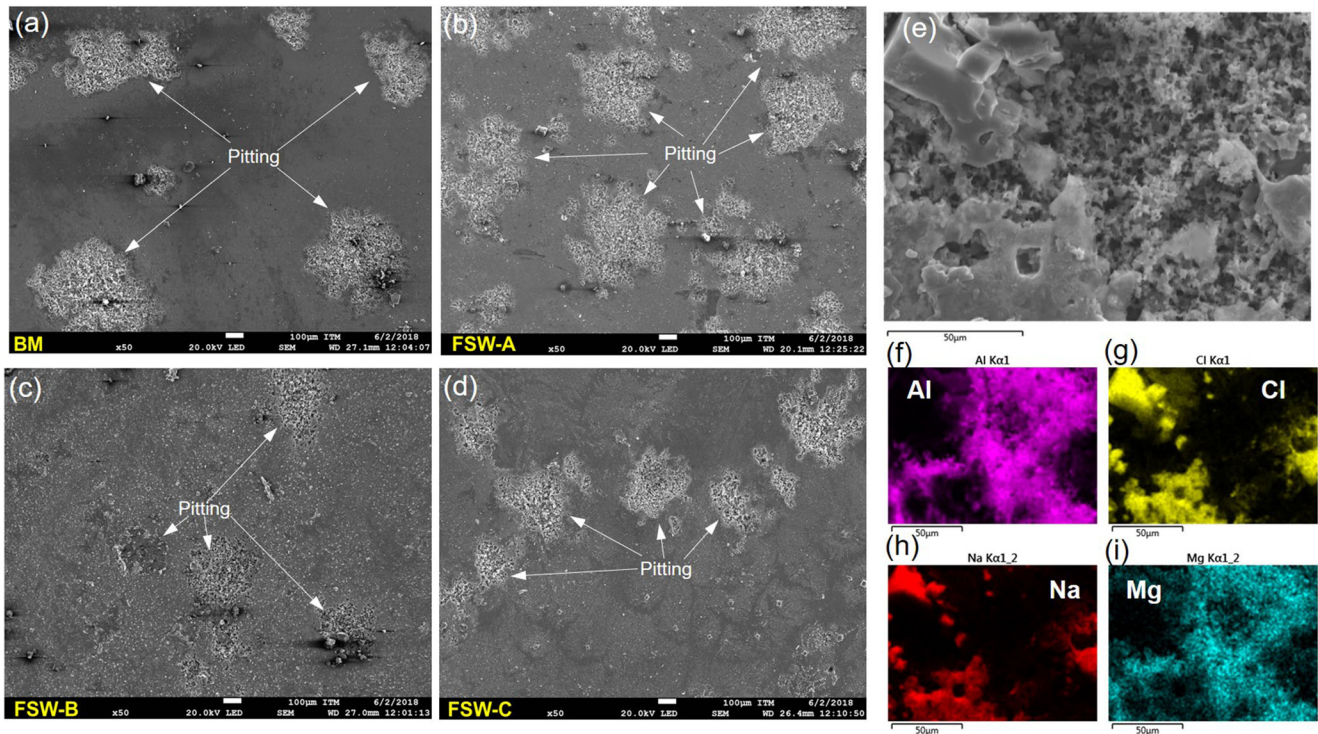
Fig. 10 Electron microscopy images show pitting corrosion at nugget region in conditions: (a) base metal, (b) FSW-A, (c) FSW-B, (d) FSW-C. Analysis of pit region (e) morphology with BSE image mode shows NaCl crystals. Chemical composition mapping (f) Al, (g) Cl, (h) Na, and (i) Mg

typical behavior for a metal electrolyte interface. A clear correlation is evidenced between the increase in the speed of agitation and the impedance of the metal surface, which is associated with the increase in the diameter of the dome, as well as the increase in height. The abovementioned is confirmed by adjusting the impedance spectra to the electric circuit model. As can be seen in Table 5, the CPE-P values are between 0.89 and 0.90, which indicates that the interface presents a highly capacitive behavior; this type of behavior is associated with the homogeneity of the surface and the presence of a protective oxide layer. Likewise, the high values of resistance R shown in Table 5 allow to corroborate the good behavior against corrosion that was previously described in the Tafel analysis. Finally, in Fig. 10, the scanning electron microscopy analysis of surfaces at stirred region compared to base metal after corrosion attack is shown. It can be observed that there are pitting corrosion preferential attacks in grain boundaries, which progressively were decreasing in extension when both ratio $\omega \cdot v^{-1}$ and heat input decreased, coinciding with grain refinement. Corroded area shows growth of sodium chloride probably associated to Mg-rich locations and Al_3Fe presence, and these features were also observed in welded joint obtained by C condition. The most probable explanation of this is due to galvanic coupling between these noble intermetallic precipitates and Al-Mg-rich matrix; this behavior was observed in other works [25, 36, 37].

4 Conclusions

In this work, the effects on corrosion behavior of process parameters used during friction stir welding of AA5052-H32 were studied. Based on the obtained results, the following remarkable conclusions are extracted:

•High deformation promoted by FSW in a strengthened material as AA5052-H32 lead to high heat both plasticizer and frictional, which could to carry out excessive grain coarsening in stirred region, decreasing mechanical and corrosion resistance.

•Appropriated combination of rotational and traverse speed using featured shoulder tools could modify both heat flow and degree of deformation, varying the microstructure conditions in stirred region of welded joints regarding tools without those characteristics. Specially, it was observed that when heat input and ratio $w \cdot v^{-1}$ were decreased then resistance corrosion was increased, producing simultaneously acceptable mechanical properties.

•The best results of corrosion behavior in stirred region of welded joints were obtained with parameter combination of 700 rpm and 100 mm·min^{-1} (–C Condition) which produced adequate mechanical properties in AA5052-H32 alloys; nevertheless, improvement of welding practice should be made aiming to reduce possible flaws in those welded joints.

Author contribution R. Soto Díaz and A. Sandoval fabricated the samples and carried out the experiments. J. Unfried-Silgado conceived the original idea, supervised the project, and wrote the manuscript with support from R. Soto Díaz and A. Sandoval.

Declarations

Ethics approval The submitted work is original and it not has been published elsewhere in any form or language.

Consent to participate This research did not involve using of living beings (humans or animals) or organisms or anything vegetable species nor voluntary or involuntary participation in activities that cause detrimental or defamatory on humans in all experimental activities.

Consent for publication Not applicable.

Conflict of interest The authors declare no competing interests.

5.References

1. Anand Sekhar R (2019) Determining the formability of AA5052 sheets in annealed and H32 condition. https://doi.org/10.1088/1742-6596/1355/1/012044

2. Wang B, Chen XH, Pan FS, Mao JJ, Fang Y (2015) Effects of cold rolling and heat treatment on microstructure and mechanical properties of AA 5052 aluminum alloy. Trans Nonferrous Met Soc China English Ed. https://doi.org/10.1016/S1003-6326(15)63866-3

3. Shanavas S, Raja Dhas JE (2017) Weldability of AA 5052 H32 aluminium alloy by TIG welding and FSW process - a comparative study. https://doi.org/10.1088/1757-899X/247/1/012016

4. Kim SJ, Jang SK, Han MS, Kim SK, Kim JS (2011) Effects of precipitation strengthening heat treatment for Al-Mg alloy. Trans Nonferrous Met Soc China English Ed. https://doi.org/10.1016/S1003-6326(11)60845-5

5. Yogesha KK, Joshi A, Jayaganthan R (2017) Fatigue behavior of ultrafine-grained 5052 Al alloy processed through different rolling methods. J Mater Eng Perform. https://doi.org/10.1007/s11665-017-2705-8

6. T. E. M. D. S. George, *Handbook of aluminum volume 1 physical metallurgy and processes*. 1969.

7. Davis JR (2001) Light metals and alloys-aluminum and aluminum alloys. Alloy Underst Basics

8. Scotti A, da Silva CLM (2006) The influence of double pulse on porosity formation in aluminum GMAW. J Mater Process Technol

9. Sarmast A, Serajzadeh S (2019) The influence of welding polarity on mechanical properties, microstructure and residual stresses of gas tungsten arc welded AA5052. Int J Adv Manuf Technol. https://doi.org/10.1007/s00170-019-04580-7

10. Zhang DQ, Park YW, Lee KY (2009) Corrosion behaviors of ND: YAG laser-GMA hybrid weldment of AA5052-H32 Al alloys. Surf Rev Lett. https://doi.org/10.1142/S0218625X09012275

11. Abbasi M, Givi M, Bagheri B (2020) New method to enhance the mechanical characteristics of Al-5052 alloy weldment produced by tungsten inert gas. Proc Inst Mech Eng Part B J Eng Manuf. https://doi.org/10.1177/0954405420929777

12. Nur R, Sultan AZ, Suyuti MA (2017) Mechanical properties on friction stir welding of aluminum alloy 5052. ARPN J Eng Appl Sci

13. Kwon YJ, Shim SB, Park DH (2009) Friction stir welding of 5052 aluminum alloy plates. Trans Nonferrous Met Soc China English Ed. https://doi.org/10.1016/S1003-6326(10)60239-7

14. Reddy NR, Reddy GM (2016) Friction stir welding of aluminium alloys - a review. Int J Mech Eng Technol

15. Ma ZY, Feng AH, Chen DL, Shen J (2018) Recent advances in friction stir welding/processing of aluminum alloys: microstructural evolution and mechanical properties. Critical Reviews in Solid State and Materials Sciences. https://doi.org/10.1080/10408436.2017.1358145

16. Lim Y-B, Lee K-J (2019) Microtexture and microstructural evolution of friction stir welded AA5052-H32 joints. J Weld Join. https://doi.org/10.5781/jwj.2019.37.2.6

17. Tufaro LN, Manzoni I, Svoboda HG (2015) Effect of heat input on AA5052 friction stir welds characteristics. Procedia Mater Sci. https://doi.org/10.1016/j.mspro.2015.04.152

18. Cuellar KJQ, Silveira JLL (2017) Analysis of torque in friction stir welding of aluminum alloy 5052 by inverse problem method. J Manuf Sci Eng Trans ASME. https://doi.org/10.1115/1.4035719

19. Totten G E and MacKenzie D S, *Volume 2: alloy production and materials manufacturing*. 2003

20. Gupta AK, Yadav SK (2018) Experimental investigation of friction stir welding on AA 5052 H32. Int J Appl Eng Res 13(12):10365–10371

21. Shanavas S, Dhas JER (2018) Weld quality prediction of AA 5052-H32 aluminium alloy using neural network approach. https://doi.org/10.1016/j.matpr.2017.11.516

22. Gudic S, Vrsalovic L, Kliškic M, Jerkovic I, Radonic A, Zekic M (2016) Corrosion inhibition of AA 5052 aluminium alloy in NaCl solution by different types of honey. Int J Electrochem Sci

23. Wang D, Yang D, Zhang D, Li K, Gao L, Lin T (2015) Electrochemical and DFT studies of quinoline derivatives on corrosion inhibition of AA5052 aluminium alloy in NaCl solution. Appl Surf Sci. https://doi.org/10.1016/j.apsusc.2015.09.206

24. Shamsudeen S, John ERD (2019) Effect of welding on pitting and intergranular corrosion behavior of marine grade aluminum alloy. Mater Perform Charact. https://doi.org/10.1520/MPC20180118

25. Bagheri Hariri M, Gholami Shiri S, Yaghoubinezhad Y, Mohammadi Rahvard M (2013) The optimum combination of tool rotation rate and traveling speed for obtaining the preferable corrosion behavior and mechanical properties of friction stir welded AA5052 aluminum alloy. Mater Des. https://doi.org/10.1016/j.matdes.2013.03.027

26. Reis FM, De Melo HG, Costa I (2006) EIS investigation on Al 5052 alloy surface preparation for self-assembling monolayer. https://doi.org/10.1016/j.electacta.2005.02.118

27. de Andrade JS, Vieira MRS, Oliveira SH, de Melo Santos SK, Urtiga Filho SL (2020) Study of microbiologically induced corrosion of 5052 aluminum alloy by sulfate-reducing bacteria in seawater. Mater Chem Phys. https://doi.org/10.1016/j.matchemphys.2019.122296

28. Unfried-Silgado J, Torres-Ardila A, Carrasco-García JC, Rodríguez-Fernández J (2017) Effects of shoulder geometry of tool on microstructure and mechanical properties of friction stir welded joints of AA1100 aluminum alloy. DYNA 84(200). https://doi.org/10.15446/dyna.v84n200.55787

29. Arbegast WJ (2008) A flow-partitioned deformation zone model for defect formation during friction stir welding. Scr Mater. https://doi.org/10.1016/j.scriptamat.2007.10.031

30. Chang WS, Cho HJ, Kim HJ, Chun CK (2007) Evaluation of friction spot joining weldability of Al alloys for automotive. Mater Sci Forum 539-543:411–416. https://doi.org/10.4028/www.scientific.net/msf.539-543.411

31. Dialami N, Cervera M, Chiumenti M, Segatori A (2019) Prediction of joint line remnant defect in friction stir welding. Int J Mech Sci. https://doi.org/10.1016/j.ijmecsci.2018.11.012

32. W. J. Kyffin, "FSW as a repair technique for surface cracks in stainless steel," 2007.

33. A. Rollett, F. Humphreys, G. S. Rohrer, and M. Hatherly, *Recrystallization and related annealing phenomena: Second Edition*. 2004.

34. Mishra RS, Ma ZY (2005) Friction stir welding and processing. *Materials Science and Engineering R, Reports*. https://doi.org/10.1016/j.mser.2005.07.001

35. Barla M, Jaidi J (2018) Influence of strain hardening behaviour in friction stir welded joints of aluminium-alloy plates. https://doi.org/10.1016/j.matpr.2017.11.639

36. Du B et al (2020) Effect of extrusion process on the mechanical and in vitro degradation performance of a biomedical Mg-Zn-Y-Nd alloy. Bioact Mater. https://doi.org/10.1016/j.bioactmat.2020.02.002

37. Krawiec H, Szklarz Z, Vignal V (2012) Influence of applied strain on the microstructural corrosion of AlMg2 as-cast aluminium alloy in sodium chloride solution. Corros Sci. https://doi.org/10.1016/j.corsci.2012.08.047